Microwave Photonic Direction-Finding Spectrometer

William L. Beardell, *Graduate Student Member, IEEE*, Conor J. Ryan, Garrett J. Schneider, Janusz Murakowski, and Dennis W. Prather, *Fellow, IEEE*

***Abstract*—In this paper, we propose an architecture wherein the radio-frequency (RF) field at the antenna array is up-converted to an optical carrier and passed through an array of optical fibers, after which an analog Fourier transform is taken in a free-space optical processor. Through the use of multiple temporal dispersion projections, implemented through varied-length optical fiber segments, the locations of RF sources in three-dimensional space spanning angle-of-arrival (AoA) and instantaneous frequency may be determined on a millisecond time scale using commercial computing hardware after detection by a charge-coupled device (CCD) camera. We present a mathematical formulation of the problem, followed by simulated and experimental results showing three-dimensional spatial-spectral localization through the solution to a system of equations brought forth through the use of Fourier optics to process the RF field.**

***Index Terms*—Optical signal processing, microwave photonics, millimeter wave communication, multispectral imaging, spatial diversity.**

I. Introduction

PROVISIONS for future wireless networks are driven by the need for ever-increasing data rates [1], [2], [3]. To address this, emerging wireless networks are increasing their carrier frequencies to the millimeter-wave (mmW) regime, where the hardware requirements in terms of cost, size, weight and power (C-SWAP) to perform the digital beam-forming process become quite demanding. Digital beamforming, along with digital beamspace processing techniques such as BLAST and MUSIC, allow for angle-of-arrival (AoA) and frequency determination and are extensively implemented in the field [4], [5], [6]. However, digital beamforming techniques generally rely upon recording of high-frequency signals, implemented through high-speed analog-to-digital converters (ADCs). To handle today's broadband data streams, these ADCs have become quite expensive and power-hungry; techniques such as front-end downconversion reduce the required sample rates while introducing local oscillator (LO) synchronization error [7]. Further, performing direction-finding and frequency measurement requires either matrix inversions or fast Fourier transforms, with both operations becoming increasingly complex as array size increases. Additional techniques such as RF lenses alleviate the computational cost of the beamforming step, but are bulky due to their necessary RF wavelength-scale footprint, and can be lossy depending upon the material system [8], [9]. Array windowing or subarray processing offers a reduction in the number of recorded data streams, albeit by creating a trade-space of complexity versus beamforming capability [10], [11].

Optical beamforming addresses many of these concerns by moving the beamforming process to a free-space optical processor, in which an optical lens performs an analog Fourier transform of a scaled version of the RF phase front incident upon the antenna array [12], [13], [14], [15], [16]. This operation is performed at the speed of light, with detection performed by either a charge-coupled device (CCD) camera, or, in the presence of a coherent optical local oscillator, by photodetectors, which may be high-speed for high signal data rates [17], [18]. Previous investigations have demonstrated instantaneous angle-angle [12], [15], [16] and angle-frequency [19] source localization, while three-dimensional imaging has, to this point, been implemented through complex algebraic reconstruction algorithms and a tomographic approach [20], [21], requiring a library of resolvable source coordinates in angle-angle-frequency space, with size determined by the product of the field-of-view (FOV) and operating bandwidth divided by spatio-temporal resolution [22]. This reconstruction technique becomes prohibitively complex for wideband, high-resolution systems, and therefore may take advantage of similar compressive sensing techniques to those used in digital beamforming [23].

The need for fast and accurate channel identification and source location has grown due to the opening of mmW spectrum for 5G ultrawideband (5G UWB) communication networks, which has grown to include wideband imaging systems. The approach detailed in [19] presents an instantaneous identification of source azimuth and frequency, while the preservation of a linear phase front allows for the application of heterodyne signal recovery techniques due to the confinement of RF power to one optical beam for each source [18].

In this work, we use the array shown in Fig. 1 to extend the instantaneous two-dimensional spatial-spectral channelization technique presented in [19] to instantaneous spatial-spectral

Manuscript received 18 July 2022; revised 24 October 2022, 15 December 2022, and 21 January 2023; accepted 1 February 2023. Date of publication 6 February 2023; date of current version 16 May 2023. This work was supported by the Air Force Research Laboratory contract under Grant FA8750-18-C-0182. *(Corresponding author: William L. Beardell.)*

William L. Beardell is with the University of Delaware, Electrical and Computer Engineering, Newark, DE 19716 USA (e-mail: beardell@udel.edu).

Conor J. Ryan is with the Ball Aerospace and Technologies Corporation, Broomfield, CO 80021 USA (e-mail: cjryan@udel.edu).

Garrett J. Schneider and Dennis W. Prather are with the University of Delaware, Electrical and Computer Engineering, Newark, DE 19716 USA, and also with the Ball Aerospace and Technologies Corporation, Broomfield, CO 80021 USA (e-mail: gschneid@UDel.Edu; dprather@udel.edu).

Janusz Murakowski is with the Phase Sensitive Innovations, Inc., Newark, DE 19713 USA (e-mail: jam@udel.edu).

Color versions of one or more figures in this article are available at https://doi.org/10.1109/JLT.2023.3242627.

Digital Object Identifier 10.1109/JLT.2023.3242627

Fig. 1. Two-dimensional antenna array with aperiodic antenna positions for alias-free imaging.

imaging in three dimensions, fully characterizing the locations of emitters in signal frequency and azimuthal and elevation angles of arrival (AoA), referred to in this paper as $(\omega_{\text{rf}}, \theta_{\text{az}}, \theta_{\text{el}})$ space, with reference to the RF angular frequency ω_{rf} and the azimuthal and elevation angles, respectively. The direction-finding spectrometer improves upon the tomographic method by using a simple system of three equations to determine the three unknown source variables, resulting in hyperspectral source identification n the order of 1 ms, an enabling technology for spatial-spectral filtering and signal recovery [24], [25]. While the approach presented herein is restricted to time-duplexed scene acquisiton with multiple time delay profiles, the underlying approach consisting of a solution of three simple equations with three unknowns, combined with commercially-available kHz-speed CCD cameras and modern FPGA and GPU computing architectures, should enable a significant improvement in signal identification speeds over existing techniques.

The contents of this paper are organized as follows: we first present a brief discussion of the mathematical principles of the approach in Section II, followed by a simulation to test the approach in Section III. The experiment, including an overview of the setup, followed by a presentation of results, is presented in Section IV, and a short summary and concluding remarks are given in Section V.

II. Mathematical Basis and Principle of Operation

Shown in Fig. 2 is an abstract illustration of system construction. Plane waves impinge upon the antenna array, inducing a phase at each antenna element within the array that is proportional to the frequency and angle-of-arrival (AoA) of each incoming wave. The output of each antenna feeds a low-noise amplifier, which in turn drives the RF input of an electro-optic phase modulator, thereby upconverting the sampled RF field to an optical field in the optical C-band. Typically, the optical field at the output of the modulators is propagated through an array of fibers, resulting in an optical field that is a scaled version of the RF field being launched into the free-space optical processor. Additionally in this work, a fiber arrayed waveguide grating (FAWG) results in passive steering of this scaled phase front exclusively as a function of frequency. The FAWG introduces true-time delays t_n linearly proportional to vertical antenna position r_{ny} through the scaling factor s', as will be discussed in this Section. In the free-space optics, the optical field first passes through a polarizing beam-splitter and a quarter-wave plate, at which point the polarization is changed from linear to circular. Following the quarter-wave plate, a series of Dense Wavelength Division Multiplexing (DWDM) filters reflects the optical carrier from each fiber, after which point the quarter-wave plate turns the circular polarization into a wave polarized linearly and orthogonal to the original input. Thereafter, it is redirected to a separate arm for overlay with a common reference of swept phase to determine phase perturbations incurred through propagation along the optical fiber. As a result, the RF phase front is faithfully represented by the optical field [26], [27]. At the other output of the beamsplitter, the DWDM filters allow the RF sidebands upon the optical carrier to continue on to a biconvex spherical lens of focal length f, which performs optically a spatial Fourier transform of the input field. The resulting image is then sampled by a charge-coupled device (CCD) camera sensitive to 1.55 μm radiation, thereby allowing optical imaging of the RF beamspace.

A. Spatio-Temporal Arrays

The array geometry implemented in this work follows an aperiodic five-arm spiral distribution, which spreads the side-lobe power evenly throughout the field-of-regard, as described in [15]. While Fig. 2 contains a conceptual depiction of a generic antenna arrangement, a frontal view of the specific aperiodic aperture used herein is shown in Fig. 3(a). Fig. 3(b) contains the calculated point spread function (PSF) of this array, which is the response of the system to an incident plane wave; note the evenly spread-out side lobes and absence of grating lobes. The mathematical formulation of the PSF for our system is presented in Section II-C. As will be discussed in the following analysis, the relative time delay in fiber is linearly proportional to the vertical position of each antenna within the array, which results in a temporal array that is also aperiodic. While this work considers these aperiodic spatio-temporal arrays, the following analysis holds for periodic arrays for both 2D spatial arrays as well as time delay profiles, with similar trade-offs for the sampling of temporal baselines as have been extensively studied for spatial sampling. The specific array geometry used in this work was originally designed for use in previous investigations [19], [20], [28] and was retained here for the sake of continuity and convenience. A trade-space study investigating the merits and drawbacks of various array geometries with the added context of temporal sampling may prove fruitful, but is beyond the scope of this work.

B. System Layout

As shown to the left in Fig. 2, an incident plane wave with spatial frequency $k = |\mathbf{k}| = \omega_{\text{rf}}/c$ and an oblique incidence angle θ creates a phase distribution across the antenna array determined by the frequency of the wave $\omega_{\text{rf}} = 2\pi f_{\text{rf}}$, specified by azimuth (θ_{az}) and elevation (θ_{el}), and antenna positions $\mathbf{r}$. The

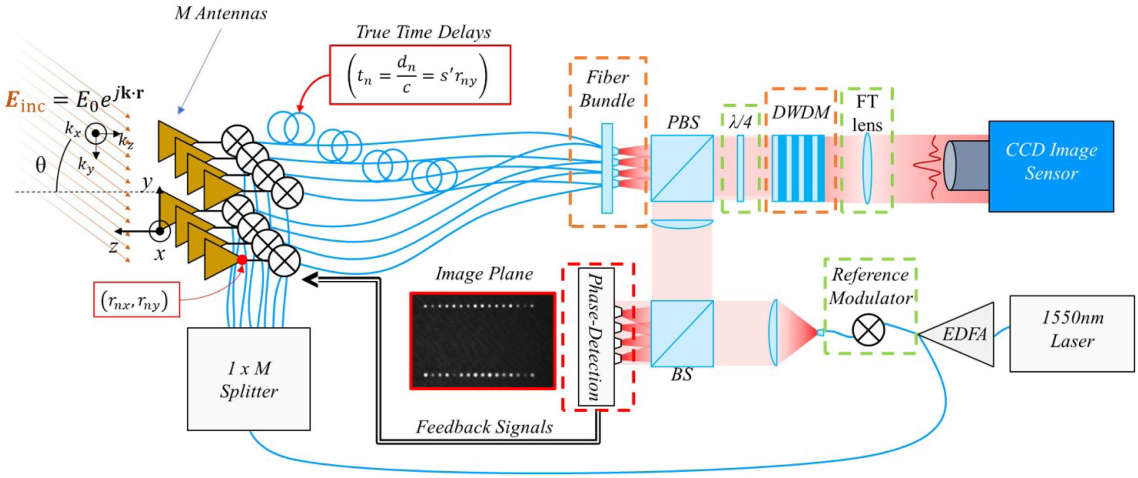

Fig. 2. Abstract illustration of far-field plane wave incidence upon an antenna array in the x-y plane followed by up-conversion and free-space optical imaging. The angle θ in this case corresponds to the elevation angle θ_{el}. The elements of the array used in this work are distributed along the x axis as well, allowing for the encoding of phase information corresponding to horizontal AoAs, denoted by θ_{az}. The antenna array depicted is simplified for illustrative purposes; the specific array used in this work takes an aperiodic arrangement of thirty elements, and is shown in Fig. 3(a). PBS: Polarizing Beam Splitter; BS: Non-Polarizing Beam Splitter; $\lambda/4$ = Quarter-Wave Plate; DWDM = Dense Wavelength Division Multiplexing optical filters; EDFA: Erbium-Doped Fiber Amplifier; CCD: Charge-Coupled Device camera.

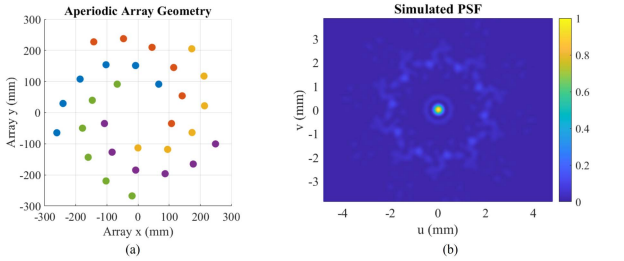

Fig. 3. (a) Illustration of distributed aperture RF array used in this work. The spiral structure is highlighted by plotting each of the five arms in a different color. Five-arm spiral geometry designed for uniform distribution of side-lobes across the element-defined field-of-view (FOV) of 10°. (b) Simulated normalized optical point-spread function (PSF) as measured by CCD camera showing distribution of side-lobes, but not grating lobes, across entire FOV.

phase distributions across the array together with the frequency ω_{rf} uniquely determine the $\mathbf{k}$-vector of each plane wave sampled by the array. The phase ϕ_n at each antenna is a dot product of the wave vector $\mathbf{k}$ and the antenna-position vector $\mathbf{r}_n$:

$$\phi_n = \mathbf{k} \cdot \mathbf{r}_n = k_x r_{nx} + k_y r_{ny} \tag{1}$$

where, per Fig. 2, the antennas are assumed to lie in the xy-plane. The x and y components of the k-vector are related to the AoAs θ_{az} and θ_{el}, respectively. The linear tapered slot antennas (LTSAs) used in this work restrict the field of view (FOV) of the system to 10° or ±5° off broadside in all directions. Within this FOV, the x and y components of the k-vectors are approximately proportional to the respective AoAs and to the frequency ω_{rf} of the incident plane wave, as discussed further in Section II-D.

The captured RF field then modulates the phase of an optical carrier of frequency ω_{opt} through a lithium niobate phase modulator located behind each antenna element. The relative phase of the optical carrier in these modulators is held constant across the array to account for phase noise incurred during propagation from the modulator to the input of the free space optical processor [26]. This phase-locking additionally allows for phase steering of the RF array by modifying the DC bias point of each modulator, allowing an arbitrary phase to be added to any channel. We consider first the case of a mmW imaging system in which all time delays from up-conversion to free-space launch are equal. In this configuration, the phase at each fiber at the input of the optical processor is solely dependent upon the RF phase as calculated in (1).

C. Point Spread Function Formulation

Through an optical Fourier transform by a lens of focal length f with optical wavelength λ as shown in the right side of Fig. 2, the spatial frequency distribution sampled by the RF array scaled by the factor s is represented in (u, v) space at the Fourier plane of the optical processor by the expression [29]:

$$\begin{aligned} U_{\text{I}}(u,v) = &\frac{U_0(u,v)}{j\lambda f} \\ &\times \sum_n A_n \exp\left[-j\left(k_x + \frac{2\pi s}{\lambda f}u\right) r_{nx}\right] \\ &\times \exp\left[-j\left(k_y + \frac{2\pi s}{\lambda f}v\right) r_{ny}\right] + \text{c.c.} \end{aligned} \tag{2}$$

where $U_0(u, v)$ represents the distribution of optical power across the Fourier plane arising from the Fourier transform of the individual fiber modes and A_n represents the sideband power present in the nth optical fiber. For the purpose of this work, all A_n are measured to be approximately equal. We use the term U_{I} to denote the field at the Fourier plane for the case where all path lengths from antenna to optical processor are identical, while we will use the term U_{F} to denote the Fourier field generated when a FAWG is inserted.

The spot location at the Fourier plane in (u, v) space for each source in the scene is defined through the projections of $\mathbf{k}$ upon the antenna array, as represented in (2). Since the antennas

are distributed in two dimensions, the array is sensitive to both azimuthal and elevation AoAs. However, since k_x and k_y depend upon both frequency and angle, for a broadband imaging system the spot location on the image plane is ambiguous. To address this, we introduce a FAWG in which the time delay in fiber from modulator to optical processor is linearly proportional to that fiber's vertical position in the array; this creates an additional phase that is exclusively proportional to the source frequency determined by the time delay in the nth fiber t_n and RF frequency ω_{rf}. As a result, the PSF at the image plane of the optical processor is steered horizontally by k_x, and vertically by both k_y as well as additionally by the frequency ω_{rf}:

$$\begin{aligned} U_{\text{F}}(u,v') = \frac{U_0(u,v')}{j\lambda f} & \\ \times \sum_n A_n \exp\left[-j\left(k_x + \frac{2\pi s}{\lambda f}u\right) r_{nx}\right] & \\ \times \exp\left[-j\left(k_y + \frac{2\pi s}{\lambda f}v'\right) r_{ny}\right] & \\ \times \exp\left[j\left(\omega_{\text{rf}} - \frac{2\pi s'}{\lambda f}v'\right) t_n\right] + \text{c.c.} & \end{aligned} \tag{3}$$

where s' is the ratio of the vertical extent of the fiber array to the time delay difference between the longest and the shortest fiber, and v' denotes the vertical coordinate of the image plane fed by both an RF array distributed in y and fiber lengths proportional to vertical antenna position. We refer to the PSF measured with a specific value of s' as a *projection* of the RF field at the array. Note that u is congruent between 2 and 3; in this work we use horizontal spot location to correlate sources between projections.

For any polychromatic imaging system, the spot location as determined individually by (2) in (u,v) space or (3) in (u,v') space is fully ambiguous with regard to the RF source coordinates $(\omega_{\text{rf}}, \theta_{\text{az}}, \theta_{\text{el}})$ as any coordinate in u corresponds to a continuum of $(\omega_{\text{rf}}, \theta_{\text{az}})$ and any coordinate in v or v' corresponds to a continuum of $(\omega_{\text{rf}}, \theta_{\text{el}})$. As will be shown in the following Section, only when both fiber profiles are used at the same time may source locations in all 3 dimensions be determined.

D. Spot Location on Fourier Plane

The formulation for PSF generation in the optical processor takes the form of a Fourier transform of the superposition of the optical fields at each fiber location in the launch plane of the optical layout. As a result, the output field in either (u,v) (for the flat profile) or (u,v') (for the FAWG) is a distribution of amplitudes and phases across the Fourier plane. When the system is properly aligned, the RF phase front modulated on the optical carrier can be thought of as a plane wave at the input of the optical processor, or notionally a constant in 'real' space, which is represented by a delta function in Fourier space. For this diffraction-limited optical system, the delta function is manifested by an envelope around the notional location of the delta function in the Fourier plane, its location determined exclusively by the in-phase condition of all elements in the fiber array and a spot size (or output waist) determined by the primary lens focal length, the optical wavelength, and the size of the input fiber array [29], [30]. For clarity, 'PSF' here refers somewhat generally to the images processed by the CCD camera representing the RF beamspace as computed by the Fourier lens.

For the imaging system presented herein, the linear tapered slot antennas used restrict the operational field-of-view to approximately ten degrees, or five degrees off broadside in any direction. Within this region, the k_x and k_y projections may be assumed to be linearly proportional to the angles θ_{az} and θ_{el}. Through simulations, the error associated with this assumption has been shown to be two orders of magnitude smaller than the resolution of the system as defined by the array diameter and maximal time delay difference. Therefore, through manipulation of (2) and (3), it can be shown that the peak location of a given PSF in (u,v) or (u,v') space follows the source coordinates through the system of equations

$$u(\omega_{\text{rf}}, \theta_{\text{az}}) = -\frac{\lambda f}{2\pi s}\frac{\omega_{\text{rf}}}{c}\theta_{\text{az}} \tag{4a}$$

$$v(\omega_{\text{rf}}, \theta_{\text{el}}) = -\frac{\lambda f}{2\pi s}\frac{\omega_{\text{rf}}}{c}\theta_{\text{el}} \tag{4b}$$

$$v'(\omega_{\text{rf}}, \theta_{\text{el}}) = \frac{\lambda f}{4\pi s}\frac{\omega_{\text{rf}}}{c}\left(\frac{s}{s_0} - 2\theta_{\text{el}}\right) - v'_d \tag{4c}$$

where $s_0 \equiv s'/c$ has been introduced to simplify analysis, and where

$$v'_d = \frac{\lambda f}{4\pi s_0 c}\omega_{\text{d}} \tag{5}$$

steers a predetermined *design* frequency ω_{d} to the center of the FAWG PSF. We have selected the design frequency to be in the center of the Ka band, taking a value of 33 GHz. The design frequency selection is implemented by the application of fixed calibration bias phases to the optical modulators, which steer a boresighted design-frequency source to the center of the CCD camera frame by canceling out the FAWG time-delay phases for that frequency [14], [19], [26].

The system (4) may be solved by identifying the optical angular frequency

$$\omega_{\text{opt}} = \frac{2\pi c}{\lambda} \tag{6}$$

and introducing a new coordinate

$$\tilde{v} \equiv 2\left(v' + v'_d - v\right) \tag{7}$$

After rearrangement of variables and unknowns, the solution to (4) takes the form

$$\theta_{\text{az}} = -\frac{s}{s_0}\left(\frac{u}{\tilde{v}}\right) \tag{8a}$$

$$\theta_{\text{el}} = -\frac{s}{s_0}\left(\frac{v}{\tilde{v}}\right) \tag{8b}$$

$$\omega_{\text{rf}} = \left(\frac{\omega_{\text{opt}} s_0}{f}\right)\tilde{v} \tag{8c}$$

for θ_{az} and θ_{el} in radians, and ω_{opt} in radians per second.

The equations (8) directly solve (4), and may be evaluated instantaneously by any modern computer. Indeed, evaluation of the expressions (8) for specific values of (u, v, v') returns source coordinates in approximately 0.5 ms. The time scale for peak detection is on the order of 1 ms, indicating that even consumer-grade computer hardware is capable of at least kilohertz-rate source detection if both fiber profiles may be measured concurrently. Further development of peak detection algorithms may significantly extend the operational capability of this approach in both speed and dynamic range, and may bear fruit in future work.

E. Principle of Operation

We obtain the measured values of u, v, and v' using a simple peak detection algorithm [31] consisting of a threshold operation followed by a low-pass filter to remove high-frequency noise from the CCD-sampled images representing the RF beamspace. This algorithm is applied to the flat-profile PSF (with coordinates u and v) and the FAWG PSF (with coordinates u and v'). As the insertion of the FAWG does not affect source location in u, we use the u coordinate to correlate pairs of peaks located in the two PSFs corresponding to the same emitter in the scene. Following peak detection, source identification is accomplished through evaluation of the system (8) through the detected values of (u, v, v'). As discussed in Section IV-C, all three terms of (8) are evaluated concurrently by readily-available commercial hardware in a combined time scale of less than one millisecond. This process is readily parallelizable as each solution can be computed concurrently, indicating that source identification time scales significantly faster than this will be readily accessible through this technique.

III. Simulated Operation

To investigate the viability of this approach, a simulated scene was generated in MATLAB using a model of the system with experimentally realizable source locations.

The simulated test case consists of two sources with $(f_1, \theta_{az1}, \theta_{el1}) = (34\,\text{GHz}, -3°, -3°)$ and $(f_2, \theta_{az2}, \theta_{el2}) = (30\,\text{GHz}, 3°, 0°)$. The associated PSF is shown in Fig. 4(a), with the detected locations of the two peaks encircled in blue and red, a convention that will continue throughout this work. The solution spaces in u for each source determined by the detected location of each peak inserted into (4a) are shown in Fig. 4(b); while the corresponding solution spaces in v (blue) and v' (red) as applied to (4b) and (4c), respectively, are shown in Fig. 4(c). As shown, the source locations are computed with extremely high accuracy. Fig. 4 is included to visualize the relationship between the CCD data space and the source coordinate space, and how the source locations in $(\omega_{rf}, \theta_{az}, \theta_{el})$ space may be computed through measurement of (u, v, v') space.

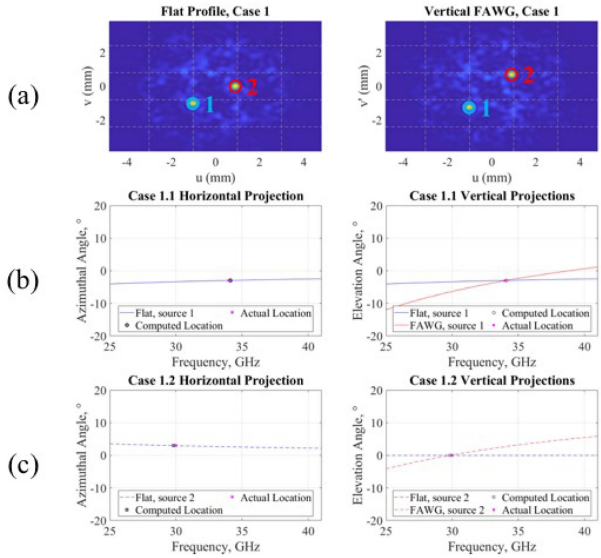

Fig. 4. (a) Simulated point-spread functions for flat (left) and FAWG (right) fiber profiles corresponding to Case 1 source distribution. (b) Solution spaces for Source 1 in (f_{rf}, θ_{az}) space (left) and (f_{rf}, θ_{el}) (right) space. (c): Corresponding solution spaces for Source 2. Solution spaces with flat fiber profile shown in blue in (b) and (c) while that for the FAWG shown in red in (c).

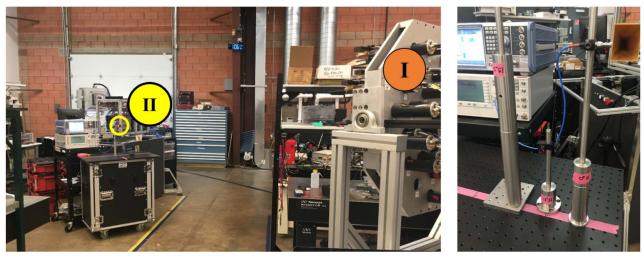

Fig. 5. (a) Experimental setup with distributed aperture antenna array (I) and single source (II) at working distance of 4 meters. (b) Antenna stands corresponding to various launch angles.

IV. Experimental Validation

A. Experimental Setup

With the approach verified using simulations, we next considered experimental validation. While the MATLAB simulations allow for the generation of PSFs corresponding to arbitrary fiber profiles, the prohibitive cost of 30 fiber splitters that would otherwise enable multiple fiber projections in real time restricts the scope of this experiment to sequential measurement of PSFs corresponding to a flat and vertical FAWG fiber profile. As a result, an experimental setup in which spatial positioning of sources is highly repeatable is necessary. To accomplish this, an optical breadboard was placed on a physically locked platform at a working distance of 4 meters from the antenna array. This arrangement is shown in Fig. 5(a). RF figures of merit such as FOV and angular resolution are determined by the geometry of the antenna array: as discussed in Section II-A, the aperiodic arrangement of receiving elements removes grating lobes and distributes side-lobes evenly across the field-of-view in the presence of constraints upon element count and angular resolution [15]. The angular resolution of $0.4°$ at the upper frequency bound of 40 GHz is determined by the 30 cm diameter of the array and the Rayleigh criterion. The operating field-of-view of this system is determined by the 3 dB beamwidth of the linear tapered slot antennas constituting the array elements,

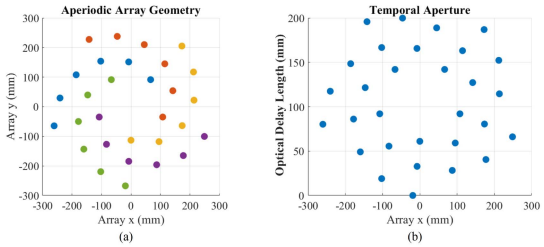

Fig. 6. (a) Illustration of the antenna element positions within the spatial aperture. (b) Illustration of the linear dependence of FAWG fiber length on the vertical position of the corresponding antenna element in the spatial aperture, which results in beam steering as a function of frequency as well as k_y.

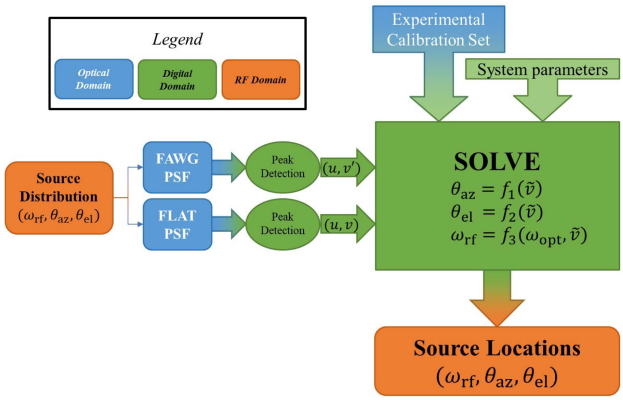

Fig. 7. Block diagram illustrating experimental validation of 3D source localization. Sources sampled with FAWG inserted and removed, followed by MATLAB program developed for peak detection and source identification using calibration set and system parameters.

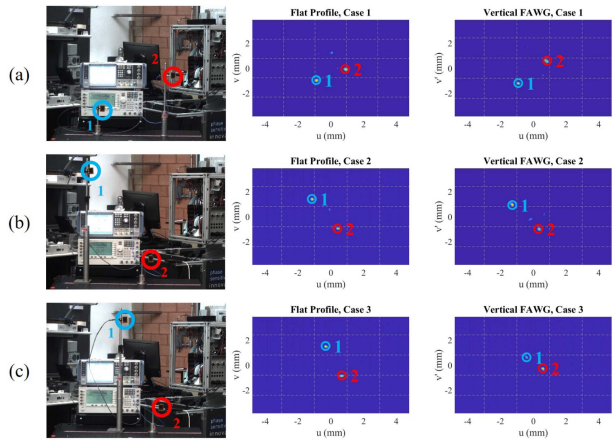

Fig. 8. Experimental source distributions. Visible images at left, with optical PSFs propagated through flat fiber profile in center and through vertically-oriented FAWG to the right for Case 1 (a), Case 2 (b), and Case 3 (c) distributions.

and extends $\pm 5^\circ$ off broadside in all directions. The spectral resolution is determined in a manner similar to the Rayleigh criterion for the angular resolution: the difference between the longest and shortest optical path length is inversely proportional to the spectral resolution, i.e. as the longest temporal basline grows the spectral resolution becomes finer [19]. Fig. 6 shows the spatio-temporal aperture: it contains side-by-side depictions of the spatial antenna arrangement, Fig 6(a), and the FAWG fiber lengths plotted versus the horizontal (x-axis) positions of the corresponding antenna elements, Fig. 6(b). The similarity of the plots illustrates the direct proportionality of the FAWG time delays to the vertical (y-axis) antenna positions. (Note that Fig. 6(a) is identical to Fig. 3; it is replicated here for ease of comparison with the temporal aperture of Fig. 6(b). For the system herein, the longest temporal baseline is approximately 18 cm in fiber, corresponding to a frequency resolution of approximately 1.5 GHz. The operating bandwidth is primarily defined by the commercial off-the-shelf RF-Lambda RLNA26G40 GB low-noise amplifiers connected to each antenna.

At a distance of 4 m from the antenna array, an increment of one degree is approximately 7 cm in the transverse plane. These markings were measured on an optical breadboard using masking tape for the azimuthal direction, while a set of three antenna stands were fabricated at fixed heights of $0^\circ, 5^\circ$, and -3° as shown in Fig. 5(b). To place a source at a given spatial position, the desired elevation stand was selected and placed such that the center of the stand base was on top of the azimuthal line. The antennas used were a matched set of WiseWave ARH2220-02 standard gain horn antennas. Comparison of PSFs with equivalent source distributions taken at different times demonstrated that this method of source placement was suitably repeatable for the purpose of the experiment. Distributions of pairs of emitters were used for the experiment to demonstrate that multiple sources may be located in **k**-space; we note that more sources may be included as well at incremental additional computational cost.

B. Data Acquisition

At this stage, with repeatable source placement achieved, we begin the experimental validation of 3D source localization following the diagram shown in Fig. 7. As discussed, constraints have limited the scope of this work to sequential acquisition of each set of source distributions, first with the FAWG inserted (the resting state of this imaging system), followed by removal of the FAWG and reacquisition of the same set of distributions with a flat fiber profile. While this process incurs a time penalty through the disconnecting and reconnecting of fibers, we note that a network of 1x2 fiber splitters, with one placed at the output of each phase modulator in the front-end, would allow for simultaneous acquisition of two fiber profiles, bringing the localization time down to that necessary to perform peak detection and solve the system of equations, currently a sub-millisecond time scale.

For test cases, true coordinates have been given in triplets, formatted as $(f_{\mathrm{rf}}, \theta_{\mathrm{az}}, \theta_{\mathrm{el}})$. Visual images of the three emitter distributions are shown in the left-hand column of Fig. 8, while the measured PSFs for the three test cases with both the flat fiber profile as well as the vertically oriented FAWG are shown in the center and right columns of the same figure.

C. Discussion of Experimental Results

A summary of results is found in Table I. All sources have been reconstructed to on the order of the system resolution: 1.5 GHz spectral and, at finest, 0.4° spatial at 40 GHz as defined by the extent of the RF array. Our results indicate that the

TABLE I
SUMMARY OF EXPERIMENTAL RESULTS. NOTE THAT f_{RF} IS PRESENTED IN GHZ

Case	Source 1						Source 2					
	True			Calculated			True			Calculated		
	f_{rf}	θ_{az}	θ_{el}	$\boldsymbol{f_{\mathrm{rf}}}$	$\boldsymbol{\theta_{\mathrm{az}}}$	$\boldsymbol{\theta_{\mathrm{el}}}$	f_{rf}	θ_{az}	θ_{el}	$\boldsymbol{f_{\mathrm{rf}}}$	$\boldsymbol{\theta_{\mathrm{az}}}$	$\boldsymbol{\theta_{\mathrm{el}}}$
1	34.0	$-3.0°$	$-3.0°$	**34.0**	$\mathbf{-2.8°}$	$\mathbf{-3.0°}$	30.0	$3.0°$	$0.0°$	**30.5**	$\mathbf{3.1°}$	$\mathbf{-0.3°}$
2	35.0	$-4.0°$	$5.0°$	**34.6**	$\mathbf{-3.5°}$	$\mathbf{4.3°}$	33.0	$1.0°$	$-3.0°$	**33.2**	$\mathbf{1.3°}$	$\mathbf{-2.9°}$
3	37.0	$-1.0°$	$5.0°$	**36.5**	$\mathbf{-0.9°}$	$\mathbf{4.3°}$	30.0	$2.0°$	$-3.0°$	**30.7**	$\mathbf{2.2°}$	$\mathbf{-2.9°}$

approach presented herein does not impede the functionality of the imaging system beyond the choices made through spatio-temporal array design. While the time-multiplexed sequential PSF acquisition (dictated by the prohibitive cost of fiber splitters) was quite lengthy, once the PSFs have been acquired, the time to determine the source locations is on the order of 0.5 ms in MATLAB running on a desktop with 2.5 GHz Intel Core i5 Processor and 64 GB of RAM. Runtimes for the tomographic approach increase linearly as a function of sources in the scene. In contrast, following peak identification within each PSF the approach presented herein does not necessarily scale with the number of sources, instead simply reconciling which sources are correspondent between PSFs, demonstrating a significant performance increase over existing digital beamforming algorithms [4], [5]. This increase in source reconstruction rate brings spatial-spectral identification to beyond video-rate while the reduction of the source localization problem to a solution of 3 simple equations enables potential development of algorithmic performance improvements specific to this application, with potential for further improvement.

This approach may be improved further through the inclusion of additional time-delay profiles, or perhaps a physically separate antenna array for stereoscopic sensing. However, regardless of the number of spatial arrays used, in order to disambiguate frequency from the combined spatial-spectral information encoded upon $\mathbf{k}$, at least one nonzero time-delay profile must be used. Thus, a minimum of two arrays is required for the approach. Investigations into the use of additional arrays may prove fruitful in the future to further optimize this approach. Efficient optical design may alleviate the marginal cost associated with construction of additional optical processors, which is currently the prohibitive factor associated with adding additional time-delay profiles. Such a future system may harness photonic integrated circuits, a nascent field with the potential to reduce size and power requirements by several orders of magnitude.

V. CONCLUSION

We present an approach enabling high-speed, high-accuracy spatial-spectral identification of RF signals through optical processing with frame rates of approximately 2 kHz, which is several orders of magnitude faster than demonstrated previously. While the realization of real-time imaging of multiple time-delay profiles is beyond the scope of this work due to the cost of necessary polarization-maintaining fiber splitters, the presented approach is capable of locating sources on the order of system resolution. Thus, design parameters such as spatial resolution, field-of-view and spectral resolution are unaffected by the presented approach, and remain related to array diameter, element factor, and longest temporal delay, respectively. Following detection of optical PSFs corresponding to the RF beamspace, evaluation of expressions (8) allows for direct computation of source parameters on sub-millisecond time scales. The presented approach, consisting of the solution of three simple equations, presents a significant improvement over fast Fourier transform and matrix inversion techniques, both of which become increasingly complex as array size increases; the field-of-view divided by the resolution of this system results in approximately six hundred resolvable beams, with additional complexity coming as a result of wide operational bandwidth of the system. We note that the computation of source locations is easily parallelized, as the location of any one source does not, in general, depend on the locations of any other sources. Mixing of the RF field with an optical carrier allows for lens-based beamspace processing; using inexpensive and low-loss optical fibers the optical processor may be placed some distance from the array with minimal loss of signal strength, alleviating the need for heavy and lossy RF cables to reach a digital beamforming unit. In the future, the use of photonic integrated circuits (PICs) incorporating elements such as multi-mode interferometers (MMIs), free-propagation regions, and low-loss waveguides will significantly reduce cost, size, weight and power (C-SWAP) requirements [32], [33]. Additionally, signal processing at the CCD plane may reduce peak-finding time and improve dynamic range through time-domain processing, peak tracking, and spatial filtration at the camera, further extending the operational capability of this approach. The identification of source location triplets through the process presented herein may theoretically allow additional improvements to signal-to-noise ratio (SNR) by allowing the beamformer to perform spatial-spectral filtering based on the additional knowledge gained through k-space sensing [24], [25].

Disclosures: The authors declare no conflicts of interest.

REFERENCES

[1] Ericsson Mobility Report, Ex. Ed. P. Cerwall, Eds. P. Jonsson and S. Carson. Forecasts by R. Möller. Jun. 2021.
[2] "5G Evolution – on the Path to 6G" Dr. Nishith D. Tripathi, Dr. Jeffrey H. Reed, Rohde & Schwarz White Paper, version 1.00, Feb. 2020.
[3] 5G. Americas, "The evolution of 5G towards the next G," Tech. Rep. Dec. 2020. [Online]. Available: https://www.5gamericas.org/wp-content/uploads/2020/12/Future-Networks-2020-InDesign-PDF.pdf
[4] J. Benesty, Y. Huang, and J. Chen, "A fast recursive algorithm for optimum sequential signal detection in a BLAST system," *IEEE Trans. Signal Process.*, vol. 51, no. 7, pp. 1722–1730, Jul. 2003.
[5] B.-S. Kim, Y. Jin, J. Lee, and S. Kim, "Low-complexity MUSIC-Based direction-of-arrival detection algorithm for frequency-modulated continuous-wave vital radar," *Sensors*, vol. 20, no. 15, Jul. 2020, Art. no. 4295. [Online]. Available: https://www.mdpi.com/1424-8220/20/15/4295

[6] H. Zhang, H.-C. Wu, and S. Y. Chang, "Novel fast MUSIC algorithm for spectral estimation with high subspace dimension," in *Proc. Int. Conf. Comput., Netw. and Commun*, 2013, pp. 474–478.

[7] J. R. Long, "Effects of local oscillator errors on digital beamforming," Master's thesis, Naval Postgraduate School, Monterey, CA, USA, Mar. 2016.

[8] Rogers Corporation, "RT/Duroid® 5870/5880 High Frequency Laminates," Publication #92-101, 2022.

[9] Rogers Corporation, "RO4000®Series High Frequency Circuit Materials," Publication #92-004, 2022.

[10] S. M. Perera et al., "Wideband N-Beam arrays using low-complexity algorithms and mixed-signal integrated circuits," *IEEE J. Sel. Topics Signal Process.*, vol. 12, no. 2, pp. 368–382, May 2018.

[11] N. Song, T. Yang, and H. Sun, "Overlapped subarray based hybrid beamforming for millimeter wave multiuser massive MIMO," *IEEE Signal Process. Lett.*, vol. 24, no. 5, pp. 550–554, May 2017.

[12] R. D. Martin et al., "Video rate passive millimeter-wave imager utilizing optical upconversion with improved size, weight, and power," *Proc. SPIE*, vol. 9462, May 2015, Art. no. 946209. [Online]. Available: https://www.spiedigitallibrary.org/conference-proceedings-of-spie/9462/946209/Video-rate-passive-millimeter-wave-imager-utilizing-optical-upconversion-with/10.1117/12.2177133.short

[13] R. Martin et al., "Design and performance of a distributed aperture millimeter-wave imaging system using optical upconversion," *Proc. SPIE*, vol. 7309, May 2009, Art. no. 730908. [Online]. Available: http://proceedings.spiedigitallibrary.org/proceeding.aspx?doi=10.1117/12.818858

[14] C. Schuetz et al., "Realization of a video-rate distributed aperture millimeter-wave imaging system using optical upconversion," *Proc. SPIE*, vol. 8715, May 2013, Art. no. 87150I. [Online]. Available: https://www.spiedigitallibrary.org/conference-proceedings-of-spie/8715/87150I/Realization-of-a-video-rate-distributed-aperture-millimeter-wave-imaging/10.1117/12.2016138.short

[15] T. E. Dillon et al., "High fill factor RF aperture arrays for improved passive, real-time millimeter wave imaging," *Proc. SPIE*, vol. 10642, pp. 269–277, May 2018. [Online]. Available: https://www.spiedigitallibrary.org/conference-proceedings-of-spie/10642/106420 U/High-fill-factor-RF-aperture-arrays-for-improved-passive-real/.full

[16] Y. Zhang et al., "95-GHz front-end receiving multichip module on multilayer LCP substrate for passive millimeter-wave imaging," *IEEE Trans. Compon., Packag. Manuf. Technol.*, vol. 8, no. 12, pp. 2180–2189, Dec. 2018.

[17] J. C. Deroba, G. J. Schneider, C. A. Schuetz, and D. W. Prather, "Multifunction radio frequency photonic array with beam-space down-converting receiver," *IEEE Trans. Aerosp. Electron. Syst.*, vol. 54, no. 6, pp. 2746–2761, Dec. 2018.

[18] W. Beardell, B. Mazur, C. Ryan, G. Schneider, J. Murakowski, and D. Prather, "RF-Photonic spatial-spectral channelizing receiver," *J. Lightw. Technol.*, vol. 40, no. 2, pp. 432–441, Jan. 2022.

[19] C. J. Ryan, W. L. Beardell, J. Murakowski, G. J. Schneider, and D. W. Prather, "Instantaneous microwave-photonic spatial-spectral channelization via k-space imaging," *Opt. Exp.*, vol. 29, no. 13, pp. 19928–19944, Jun. 2021. [Online]. Available: https://www.osapublishing.org/abstract.cfm?URI=oe-29-13-19928

[20] D. D. Ross, C. J. Ryan, G. J. Schneider, J. Murakowski, and D. W. Prather, "Passive three-dimensional spatial-spectral analysis based on k-space tomography," *IEEE Photon. Technol. Lett.*, vol. 30, no. 9, pp. 817–820, May 2018. [Online]. Available: https://ieeexplore.ieee.org/document/8320802/

[21] J. Murakowski, G. J. Schneider, S. Shi, C. A. Schuetz, and D. W. Prather, "Photonic probing of radio waves for k-space tomography," *Opt. Exp.*, vol. 25, no. 14, Jul. 2017, Art. no. 15746. [Online]. Available: https://www.osapublishing.org/abstract.cfm?URI=oe-25-14-15746

[22] D. Ross, "RF photonic apertures," Ph.D. dissertation, University of Delaware, Newark, DE, USA, 2018.

[23] D. D. Ross, J. Murakowski, C. J. Ryan, G. J. Schneider, and D. W. Prather, "Compressive k-space tomography," *J. Lightw. Technol.*, vol. 36, no. 19, pp. 4478–4485, Oct. 2018. [Online]. Available: https://ieeexplore.ieee.org/document/8341499/

[24] J. N. Mait, R. D. Martin, C. A. Schuetz, and D. W. Prather, "Millimeter wave imaging with engineered point spread functions," *Opt. Eng.,* vol. 51, no. 9, May 2012, Art. no. 0 91606. [Online]. Available: https://www.spiedigitallibrary.org/journals/optical-engineering/volume-51/issue-9/091606/Millimeter-wave-imaging-with-engineered-point-spread-functions/10.1117/1.OE.51.9.091606.short

[25] G. J. Schneider, J. A. Murakowski, C. A. Schuetz, S. Shi, and D. W. Prather, "Radiofrequency signal-generation system with over seven octaves of continuous tuning," *Nature Photon.*, vol. 7, no. 2, pp. 118–122, 2013. [Online]. Available: http://www.nature.com/articles/nphoton.2012.339

[26] R. D. Martin, C. A. Schuetz, D. W. Prather, and T. E. Dillon, "Controlling the phase of optical carriers," Apr. 2012. [Online]. Available: https://patents.google.com/patent/US8159737/en

[27] T. E. Dillon et al., "Optical configuration of an upconverted millimeter-wave distributed aperture imaging system," *Proc. SPIE*, vol. 7485, Sep. 2009, Art. no. 74850G. [Online]. Available: http://proceedings.spiedigitallibrary.org/proceeding.aspx?doi=doi: 10.1117/12.830493.

[28] C. Ryan, W. Beardell, J. Murakowski, D. Ross, G. Schneider, and D. Prather, "Log-periodic temporal apertures for grating lobe suppression in k-space tomography," *Opt. Exp.*, vol. 28, pp. 15969–15983, May 2020. [Online]. Available: https://www.osapublishing.org/oe/abstract.cfm?doi=doi: 10.1364/OE.392118.

[29] J. W. Goodman, *Introduction to Fourier Optics*, 4th ed. New York, NY, USA: W. H. Freeman, 2017.

[30] W. L. Beardell, "Coherent optical processors," Master's thesis, University of Delaware, Newark, DE, USA, 2020.

[31] Natan, "Fast 2D peak finder," May 16, 2021. [Online]. Available: https://github.com/adinatan/fastpeakfind/releases/tag/1.13.0.0

[32] T. Sharma et al., "Review of recent progress on silicon nitride-based photonic integrated circuits," *IEEE Access*, vol. 8, pp. 195436–195446, 2020.

[33] S. Nelan et al., "Compact thin film lithium niobate folded intensity modulator using a waveguide crossing," *Opt. Exp.*, Feb. 2022, [Online]. Available: https://opg.optica.org/oe/abstract.cfm?msid=